

## An Intrinsic Tactile Sensor for Underwater Robotics<sup>†</sup>

Gianluca Palli\* Lorenzo Moriello\* Umberto Scarcia\*  
Claudio Melchiorri\*

\* DEI - Department of Electrical, Electronic and Information Engineering -  
University of Bologna, Viale Risorgimento 2,  
40136 Bologna, Italy

**Abstract:** In this paper, a novel intrinsic tactile sensor for underwater robotic applications is presented, along with some experimental results. The sensor is based on optoelectronic components and therefore its design is quite simple and reliable. Moreover, it is suitable to be adapted to different mechanical configurations, allowing its integration in e.g. the fingers of robotic hands or on the wrist of a robot arm. In this paper, the basic principle and the design of the sensor are presented, describing also some prototypes developed for underwater applications. Experimental data are presented and discussed to illustrate the main features of the sensors.

**Keywords:** Force/Torque Sensors, Optoelectronic Sensors, Dexterous Manipulation, Intrinsic Tactile Sensors.

### 1. INTRODUCTION

In order to make a robot able to sense what surrounds and operate safely and autonomously in unstructured environments, as in the case of underwater operations, a suitable sensory equipment is necessary. For robot design to perform recovery and assembly tasks, grasping and manipulation are key problem to be faced, and the sense of touch is essential to properly manipulate objects. The huge amount of work in tactile sensing literature also highlights the importance of having a proper sensing of the contact forces exerted during manipulations. Despite the large number of devices and the variety of solutions, the design of reliable and accurate tactile sensors has proven to be very hard, and relatively few commercial devices are currently available, mainly due to high manufacturing complexity, poor reliability and cost. Moreover, the isolation and corrosion problems typical of the marine environment represent a challenging aspect for any electronic device, and in particular for tactile sensors, further limiting their applicability in the field of underwater robotics.

Many different designs and almost every kind of physical transduction principle have been proposed for the implementation of tactile sensors. A recent and complete review on tactile sensor technologies and features is reported e.g. in Dahiya et al. [2010]. With particular reference to optical-based devices, a very common technology is based on **Fibre Bragg Gratings (FBG)**, that exploits the relationship between the variations of the FBG wavelength and the external force applied to the FBG [Heo et al., 2006]. Other well known optical tactile sensors are based on **CCD or CMOS camera to capture the deformation of a surface caused by external force** [Kamiyama et al., 2005]. Both these technologies are expensive, difficult to integrate into complex robotic structures (e.g. anthropomorphic hands, robotic arms) and involve **high computational costs**. Other clever solutions based on discrete optoelectronic components

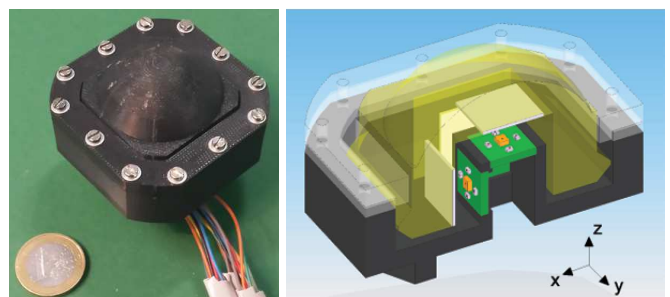


Fig. 1. The optoelectronic sensor and its CAD representation.

exploit the scattering or the reflection of a light beam. In E. Torres-Jara [2006] and G. Hellard [2002], the light beam of an light emitting diode (LED) is scattered by a silicon dome and a urethane foam cavity respectively. The working principle relies on the compression of the dome or the cavity due to applying an external force, causes a scattered energy density variation that is detected by several **PhotoDetectors (PDs)**. Hirose and Yoneda [1990] adopted a 2-axes photosensor for the implementation of an optical 6-axes force/torque sensor. In De Maria et al. [2012] a matrix of LED/PD couples is covered by a deformable elastic layer. In that case, the working principle is the union of cavity scattering principle mentioned before, and of a taxel-based reconstruction typical of CMOS sensors. In Tar and Cserey [2011] an example of a tactile/force sensor which exploits the reflection of a light cone from a LED on a silicon rubber dome is described. In this device, the force reconstruction is related to the spatial distribution of the radiation intensity after the reflection of the light on the deformable dome above the optical components.

The **6-axes force/torque (F/T)** sensor presented in this paper exploits the optical reflection concept mentioned above in order to obtain an easily **scalable and low cost intrinsic tactile sensor**. The proposed sensor is characterized by a natural robustness with respect to electromagnetic noise due to the adoption of optoelectronic components, and requires an extremely simple and compact conditioning electronics, making it easy to inte-

\* This work is supported by the Italian National Project MARIS "Marine Autonomous Robotics for InterventionS".

<sup>†</sup>Patent pending.

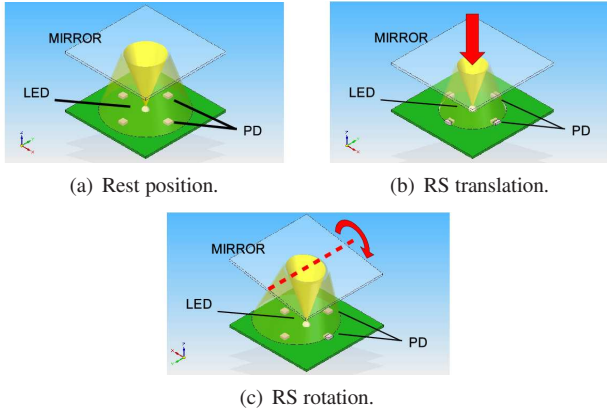


Fig. 2. Ideal propagation of the light cone emitted by the LED.

grate the sensor into complex robotic structures such as robotic hands. Moreover, the proposed sensor exploits the compliance of the o-rings used for isolating the sensible elements and the conditioning electronics from water to provide the mechanical structure the compliance needed for the implementation of the force sensors, avoiding in this way the introduction of a purposely designed compliant structure as for conventional force sensors. This solution allows both to achieve a significant simplification of the mechanical design and to reduce the dimensions of the sensor itself.

This paper is structured as follows. In Sec. 2 the principle of the sensor is described and the design of a prototype reported. Note that the developed sensor is going to be installed on a three-fingered gripper for underwater tasks, and therefore some design choices have been conditioned by this particular application. In Sec. 3 experimental results are described and discussed, while Sec. 4 concludes with final remarks and plans for future activity.

## 2. SENSOR CONCEPT AND DESIGN

The proposed sensor working principle relies on the modulation of a PD current caused by the variation of the received light power. The light is generated by an infrared source such as an LED. In the proposed sensor, the light power variation is caused by the changes of both the angle of view and the length of the optical path between the optoelectronic components induced by the relative motion of a reflecting surface under the effect of the external force to be measured [Kasap, 2001]. Assuming a single LED and a certain number of PDs arranged on the same Printed Circuit Board (PCB), and a Reflective Surface (RS) disposed in front of the PCB. The PCB is fixed to the sensor frame, while the RS moves together with the contact surface of the sensor (the fingertip). A deformable element connects the fingertip to sensor frame. To optimize the mechanical design and minimize its dimensions, the compliance of the o-ring sealing elements has been exploited to implement the deformable connection between the sensor frame and the contact surface. In the tactile sensor proposed by De Maria et al. [2012] the principle is to reconstruct the applied force by measuring the motion/deformation of the elastic layer on which the reflection or scattering of light occurs. In this case, the reflective layer is not deformable, but it can move if an external force is applied. Therefore, the idea is to detect the position and orientation of the RS, and then the applied force and torque, from the light intensity measured by the PDs,

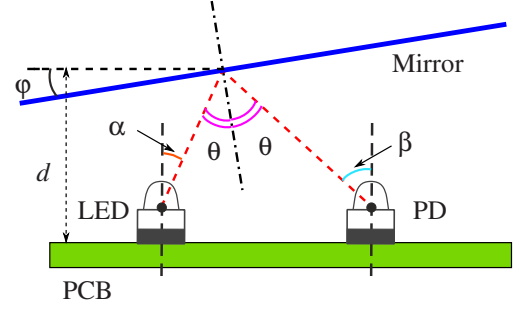


Fig. 3. Interaction between the optoelectronic components.

i.e. from the spatial distribution of reflected light cone. This principle is schematized in Fig. 2, where the distribution of the light emitted by the LED and received by the PD in case of elementary motion of the RS is shown.

### 2.1 Sensor Model and Validation

To verify the sensor design, a numerical model of the PDs current variation as a function of the distance and orientation of the RS has been developed and tested in simulation. Figure 3 shows a LED and a PD mounted on the PCB. The light path depends on the distance  $d$  and orientation  $\varphi$  of the RS. The developed model computes the light path defining first an hypothetical triangle which lies on the perpendicular plane of the RS passing through the LED and the PD, and having the reflection point, the LED, and the PD positions as corners. The model also takes into account the reflection coefficient of the RS. In Fig. 3,  $\alpha$  represents the angle between the LED mechanical axis and the segment that denotes the light path, while  $\beta$  represents the angle between the PD mechanical axis and the light path. In this state a certain amount of light emitted by the LED reaches the PD and it is proportionally converted into an electrical current,  $I_p(\alpha, \beta)$ . Recalling the theory on LED radiation patterns [Kasap, 2001], it is possible to model the interaction of the optoelectronic components. Given the radiant intensity emitted by the LED,  $\mathcal{I}(I_{LED})$  as a function of the bias current, and the geometry of the ideal light beam path (from which the angles  $\alpha$  and  $\beta$ , are calculated as mentioned before), the intensity that irradiates the PD,  $\mathcal{I}_r$ , is:

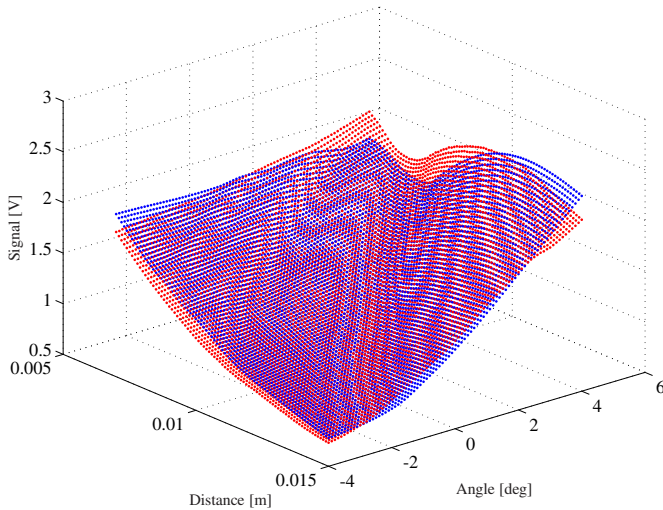
$$\mathcal{I}_r = \mathcal{I}(I_{LED}) \mathcal{L}(\alpha) \mathbb{R}\{R\} \mathcal{R}(\beta) \quad (1)$$

where  $\mathcal{L}(\alpha)$  denotes radiant intensity pattern of the LED (evaluated in  $\alpha$ ),  $\mathcal{R}(\beta)$  denotes the responsivity pattern of the PD (evaluated in  $\beta$ ) and  $\mathbb{R}\{R\}$  is the real part of the reflectivity  $R$  of the RS, that is determined by the light incidence angle with respect to the RS normal direction ( $\theta$  in Fig. 3) and the complex refractive indices  $n_1$  of the media (air) and of the RS  $n_2$  (aluminum)  $R = (R_S + R_P)/2$  where

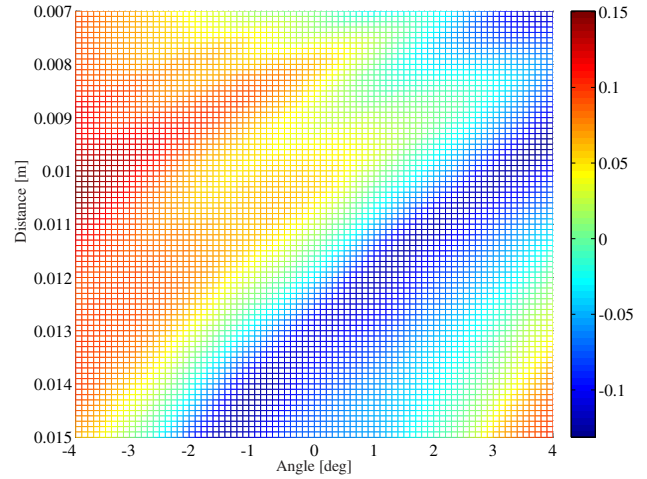
$$R_S = \left| \frac{n_1 \cos(\theta) - n_2 \sqrt{1 - \left(\frac{n_1}{n_2} \sin(\theta)\right)^2}}{n_1 \cos(\theta) + n_2 \sqrt{1 - \left(\frac{n_1}{n_2} \sin(\theta)\right)^2}} \right|^2$$

$$R_P = \left| \frac{n_1 \sqrt{1 - \left(\frac{n_1}{n_2} \sin(\theta)\right)^2} - n_2 \cos(\theta)}{n_1 \sqrt{1 - \left(\frac{n_1}{n_2} \sin(\theta)\right)^2} + n_2 \cos(\theta)} \right|^2$$

The radiant intensity pattern of the LED  $\mathcal{L}(\cdot)$  and the responsivity pattern of the PD  $\mathcal{R}(\cdot)$  are available from the data-sheets of the components. The output photocurrent  $I_{PD}$  of the PD is proportional to the incident light power  $\mathcal{E}_e$ , that is related to  $\mathcal{I}_r$  by the relation



(a) Model vs. Experiment comparison.



(b) Relative Model Error.

Fig. 4. Comparison between the theoretical model (blue) and experimental data (red) and relative model error.

$$I_{PD} = K_{PD} \mathcal{E}_e = K_{PD} \frac{A_{PD}}{\omega} \mathcal{J}_r$$

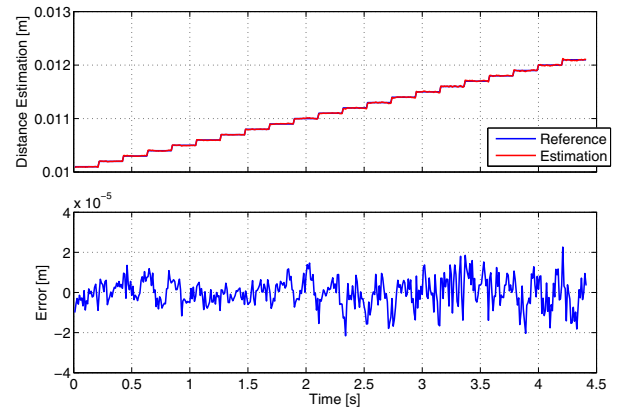
where  $K_{PD}$  is a proper constant (reported on the PD datasheet),  $A_{PD}$  is the sensitive area of the PD and  $\omega$  is the solid angle of the light cone received by the PD

$$\omega = 2\pi \left( 1 - \frac{1}{\sqrt{1 + (r/l)^2}} \right)$$

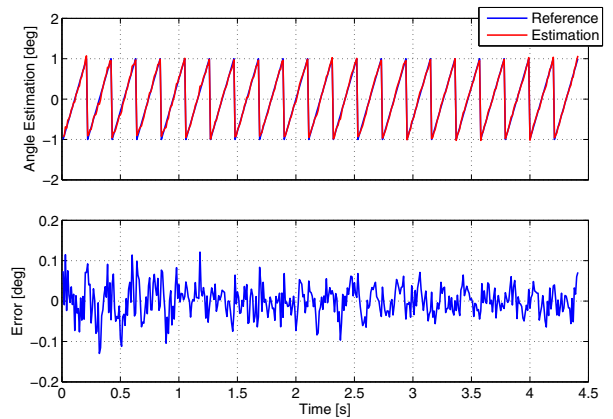
where  $l$  is the light path length and  $r = \sqrt{A_{PD}/\pi}$  is the radius of the PD area. Finally, the PD photocurrent  $I_{PD}$  is converted to an output tension by means of a resistor and measured by means of an Analog to Digital Converter (ADC).

For the experimental validation of the developed model, an infrared LED with a narrow viewing angle and with a typical peak wavelength of 850 nm (Vishay VSMY2850G) and, for the PD, a silicon NPN phototransistor (Osram SFH3010) with a maximum peak sensitivity at 860 nm wavelength have been selected. A LED/PD couple has been arranged on a printed circuit board at a distance of 6 mm, and the output voltage of the PD corresponding to different values of the RS distance and orientation has been measured. A specific laboratory setup has been built to control in a very precise way both the translations and rotation motion of the RS by means of two linear motors. In Fig. 4(a) the comparison between the experimental data and the theoretical model is reported, whereas Fig. 4(b) reports the relative error in the representation of experimental data using the theoretical model. From this figure, it is possible to see that the maximum model error is about 10% over the whole measuring range. Moreover, although the obtained characteristic is nonlinear, it is interesting to note that in a region surrounding the center of the plot (angle = 0°, distance ≈ 10 mm) the outputs of both the model and the experimental device present a very limited difference and an almost linear behavior.

Aiming at a deeper investigation on the effectiveness of the proposed sensing method, the RS position and the orientation with respect to the LED/PD plane has been reconstructed by means of a PCB with a LED and a couple of PDs symmetrically arranged with respect to the LED, reproducing the LED/PD arrangement shown in Fig. 2. The results reported in Fig. 5 show that this configuration allows to measure the distance



(a) Linear displacement.



(b) Angular displacement.

Fig. 5. Reconstruction of linear and angular displacement using a LED and two PDs.

and the orientation of the mirror with a good precision, at least for limited displacements ( $\pm 1$  deg).

## 2.2 Sensor Prototype

A LED and four PDs arranged around it equally spaced in a circle with a diameter of 6mm is the basic element of the



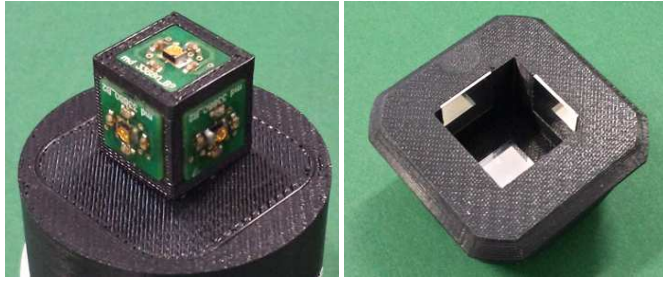


Fig. 6. Internal view of the sensor: the cube with the three electronic boards and the cover with the mirrors.

proposed force/torque sensor. This solution allows to obtain a PCB of  $1\text{ cm}^2$ . Furthermore, to be able to measure forces and torques along the three axes, 3 PCBs have been placed on three orthogonal faces of a cube, as also shown in Fig. 1 and Fig. 6, where a prototype of the sensor is shown. The PCBs have been covered by a mask with hollows for the optoelectronic components in order to avoid spurious light reflections that may negatively affect the sensor response. The relative motion of the RS and the PCBs is achieved by exploiting the o-ring seals compliance, that elastically deform when an external force is applied to the external cover of the sensor. Note that by changing these elastic elements (and in case the sensor design as well), it is possible to select the force working ranges of the sensor. This sensor is going to be placed on the fingertips of a underwater three-fingered robotic gripper [Bemfica et al., 2013] and both the dimension and some of the design choices (e.g. the o-rings for water insulation) derive from this specific application. For that purposes, the external surface of the developed sensor prototype is a sphere portion with radius  $R = 21.5\text{ mm}$ . Thanks to the intrinsic high sensibility of the selected optoelectronic components, the conditioning electronics is extremely simple and all the necessary components for acquisition and transmission of the data via a serial digital bus are integrated into the PCB. This allows a simpler integration of the sensor into the robotic gripper.

### 2.3 Characterization of O-ring Materials

The characteristics of two different o-ring materials have been evaluated by means of suitable experiments to find which material is better suited for our application. In these experiments, silicon rubber and fluorocarbon rubber o-rings have been compared by applying a sinusoidal compression with frequency range from 0.1 to 5 Hz and measuring the corresponding reaction force. The o-rings have the same dimensions in both the cases, with a thickness of 3.53 mm and an internal diameter of 47.62 mm, and both the materials present an hardness of 70 Shore A. The results reported in Fig. 7 shows that, while silicon rubber presents a quite linear response within the displacement and frequency range of our interest, fluorocarbon rubber presents a large hysteresis for high value of the compression rate. Since we are interested in a implementing a sensor whit an as wider as possible constant frequency response, the silicon o-rings are more suitable for the implementation of the proposed sensor.

## 3. CALIBRATION AND CHARACTERIZATION

For the calibration and the experimental characterization of the sensor, a laboratory setup consisting in a linear motor LinMot-

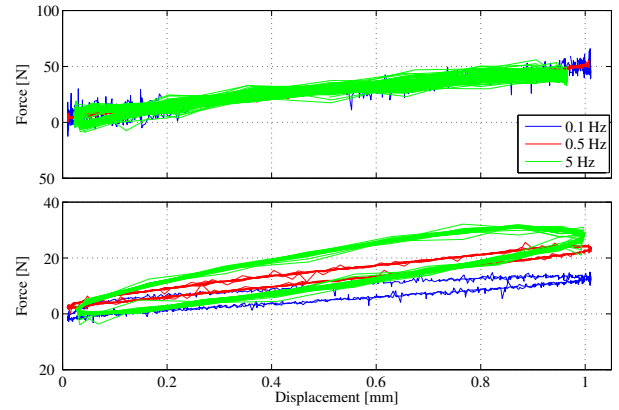


Fig. 7. Displacement/force characteristic of silicon rubber (top) and fluorocarbon rubber (bottom) o-rings for different compression rates.

37x160 equipped with a precision load cell, and an ATI Gamma SI-130-10 F/T sensor has been developed. The linear motor is used to apply the desired force to the optoelectronic force sensor along the motor axis, and is also equipped with an integrated encoder to measure the motor position. The linear motor is driven by a low-level control system that allows to apply the desired force profile compensating for the friction acting on the motor slider Palli and Melchiorri [2008]. The controller and the data acquisition system are implemented by a PC-104 with Intel ATOM processor running the RTAI-Linux realtime OS. The software design is performed using MatLab, Simulink and the Realtime Workshop by a Linux workstation, that is also used as user interface for the control and acquisition system.

### 3.1 Sensor Calibration

The calibration procedure has been performed by using as reference sensor an ATI Gamma SI-130-10 F/T sensor. The developed sensor prototype has been mounted on the reference sensor in such a way that, apart form a suitable changes in the reference frame and in the point where the force is applied, the two sensors are subject to the same force. Then a variable load in terms of both forces and torques have been applied to the sensor prototype and the data from both sensors have been acquired. The mapping between the PD output voltages and the applied force and torque vector can be done by polynomial interpolation

$$W = CV \quad (2)$$

where

$$V = [v_1^n \cdots v_{12}^n \cdots v_1 \cdots v_{12} \ 1 \cdots 1]^T$$

is the vector of the sensor output voltages (12 PD outputs), and the corresponding power up to the order of  $n$  (the ones at the end of the vector are used to remove the output offset voltage),  $W$  is the wrench vector including the three components of forces and torques

$$W = [f_x \ f_y \ f_z \ \tau_x \ \tau_y \ \tau_z]^T$$

and  $C$  is the calibration matrix that can be derived from experiments as

$$C = \Omega \Delta^+ \quad (3)$$

where  $\Delta^+$  denotes the pseudoinverse of the matrix  $\Delta$  and

$$\Omega = [W_1 \ W_2 \ \cdots \ W_i \ \cdots \ W_m]$$

$$\Delta = [V_1 \ V_2 \ \cdots \ V_i \ \cdots \ V_m]$$

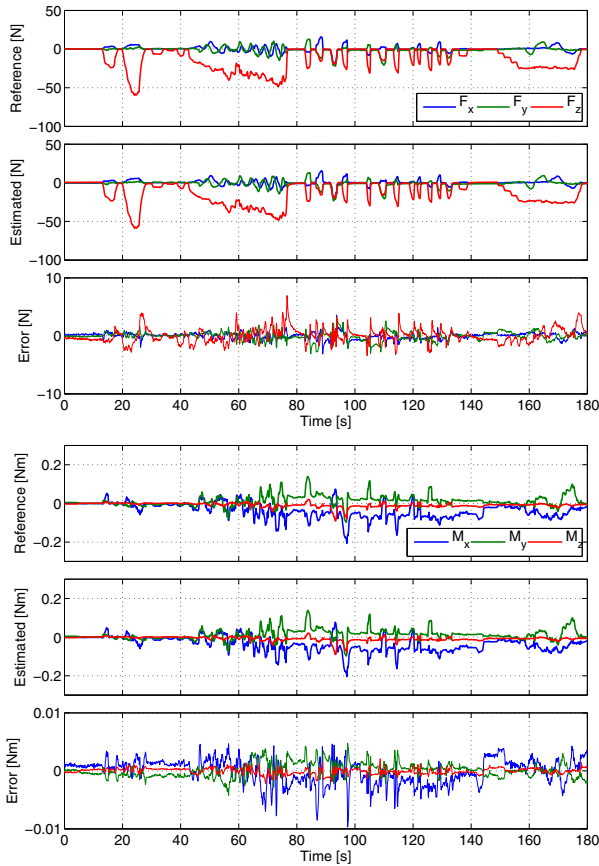


Fig. 8. Reconstruction of force and torque components.

are the matrices of the  $m$  experimental measures of the external forces/torques applied to the optoelectronic sensor and of the PD output voltages respectively. For the derivation of the calibration matrix, the force and torque components are acquired by the reference sensor and preliminary converted to the optoelectronic sensor reference frame by means of a suitable transformation matrix. A 3rd-order interpolation has been adopted for deriving the external force/torque vector from the sensor output signals because it represent a valid trade-off between computational complexity and force/torque reconstruction error. Notice that the forces are expressed in a reference frame with origin in the center of the sensor and axes direct as shown in Fig. 1. Because of the specific mechanical design<sup>1</sup>, the operating range of the sensor is  $[0 \div 100]$  N for forces along the  $z$  direction, and  $[-50 \div 50]$  N in the  $x - y$  plane, while torques are limited to  $[-5 \div 5]$  Nm along the three axes. Fig. 8 shows a test in which forces are measured by the reference sensor and by the new sensor after calibration, together with the force and torque reconstruction error. In both the cases the error is less than the 10% of the measure, showing the effectiveness of the proposed sensor.

### 3.2 Sensor performances

In order to fully characterize the sensor not only from a static point of view but to verify also its dynamic properties, a sinusoidal force with constant amplitude and varying frequency has been applied along the  $z$ -axis. The results of this experiment

<sup>1</sup> As already mentioned, the mechanical and elastic part of the sensor can be tailored for specific applications, and therefore different performances can be achieved if desired.

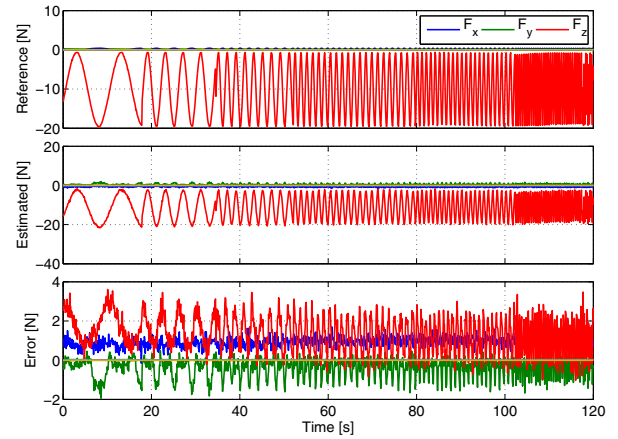


Fig. 9. Application of a sinusoidal force signal (20 N) at increasing frequencies.

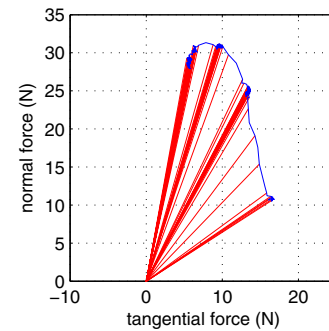


Fig. 10. Measurement of the normal and tangential forces.

are reported in Fig. 9: a 20 N sinusoidal force is applied at increasing frequencies, from 0.01 to 3 Hz. As it can be seen, the error is almost constant in the selected frequency range, fact that allows to state that the use of the sealing o-rings also as a suspension element for the implementation of the force/torque sensor does not limit the sensor performance also from the point of view of the dynamic properties.

Another experiment is reported in and Fig. 10, where a constant force along the  $z$  direction is applied to an object. An external increasing force is applied to the object as well, by means of some calibrated weights, and therefore the sensor measures both the normal ( $z$  axis) and tangential ( $x - y$  plane) forces ( $f_n, f_t$ ). In the experiment, the sensor contact surface has been covered by a silicon rubber to increase friction since the surface of the sensor, built with 3D printing technology, has a very low friction coefficient. A set of tangential force ranging from 3 to 18 N has been applied to the object, while the normal force  $f_n$  has been fixed 30 N. With a tangential force larger than 13 N, the object starts to slide, making it possible to estimate the friction coefficient  $\mu = f_t / f_n$ . This results is useful to implement a control strategies in order to avoid slippage of the object.

### 3.3 Characterization as Intrinsic Tactile Sensor

Among the many possible usages for force/torque sensors, several authors described in literature how to use them in robotic applications for the computation, besides of applied force/torque vectors, also of the contact point between e.g. the fingers of a robot hand and the grasped object, see Salisbury

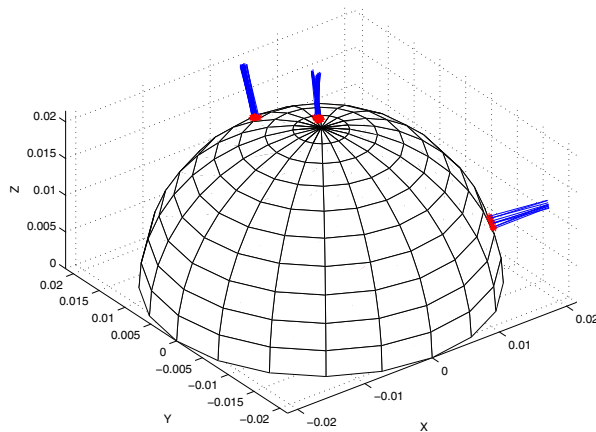


Fig. 11. Measurement of the applied forces and of the contact point.

Table 1. Results of the contact point position estimation ( $x$ ,  $y$  and  $z$  position, in mm), and corresponding sphere radius.

Actual Position	Estimated Position	Estimation Error	Radius
0.0, 1.5, 21.5	1.2, 2.1, 21.1	-1.2, -0.6, -0.1	21.2
-1.0, 10.0, 18.0	-1.4, 10.7, 18.1	0.4, -0.7, -0.1	21.1
17.0, 8.0, 6.0	17.6, 7.8, 5.4	-0.6, -0.2, 0.6	20.0

[1984], Bicchi et al. [1990], Cicchetti et al. [1995], Melchiorri [2001]. As described e.g. in Bicchi et al. [1990], in case of a sensor with spherical contact surface with radius  $R$ , the position  $p_c$  of the contact point can be obtained from the force  $f$  and torque  $m$  measured by the F/T sensor from

$$p_c = r_0 + \lambda f, \quad r_0 = \frac{f \times m}{\|f\|^2}, \quad \lambda = -\frac{1}{\|f\|} \sqrt{R^2 - \frac{\|f \times m\|^2}{\|f\|^4}}$$

Since two solution are obtained from these equations (solution of the intersection of a line with a sphere), the point for which the force is entering the surface must be selected. This principle has been applied to the proposed sensor for the estimation of the contact point of the sensor surface. Typical results are reported in Fig. 11, where the applied forces are shown as lines and the contact points are measured on the surface of the sensor. In this test, three forces are applied at three different points, and the results of the contact point estimation compared to the actual one are reported in Tab. 1. As a verification of the correctness of the results, Tab. 1 also reports the the distance of the computed contact point from the reference frame origin: it could be noticed that this value is very close to the actual value of the spherical contact surface (21.5 mm).

#### 4. CONCLUSIONS

In this paper, a novel force/torque sensor for robotic application has been presented and some preliminary results obtained with a first prototype reported and discussed. The sensor is based on optoelectronic components and therefore is a low-cost, simple and reliable device. Moreover, it is easily integrable in relatively complex devices from both the mechanical and electronic point of view. The sensor has been presented in this paper has been developed for a three-fingered gripper for underwater applications. Anyway, the proposed sensor concept has general validity and can be exploited for the implementation of force/torque sensors for other applications. The experimental

results confirm the satisfactory performances of the sensor, that can be used not only for measuring the external force/torque vector applied to it, but also as a “intrinsic” tactile sensor able to determine the position of the contact point. Further activities are in progress to characterize different elastic materials (to be used to obtain sensors with different working ranges), to identify different mechanical configurations, and to develop more compact sensors for other type of applications.

#### REFERENCES

- J. Bemfica, C. Melchiorri, L. Moriello, G. Palli, U. Scarcia, and G. Vassura. Mechatronic design of a three-fingered gripper for underwater applications. In *6th IFAC Symposium on Mechatronic Systems, Hangzhou, China*, pages 307–312, 2013.
- A. Bicchi, J.K. Salisbury, and D.L. Brock. Contact sensing from force measurements. *International Journal of Robotics Research*, 12:249–262, 1990.
- A. Cicchetti, A. Eusebi, C. Melchiorri, and G. Vassura. An intrinsic tactile force sensor for robotic manipulation. In *Proc. 7th. Int. Conf. on Advanced Robotics, ICAR’95, Sant Feliu de Guixols, Spain*, pages 889–894, 1995.
- R.S. Dahiya, G. Metta, M. Valle, and G. Sandini. Tactile sensing from humans to humanoid. *IEEE Transactions on Robotics*, 26(1):1–20, 2010.
- G. De Maria, C. Natale, and S. Pirozzi. Force/tactile sensor for robotic applications. *Sensors and Actuators A: Physical*, 175:60–72, 2012.
- R. Coral E. Torres-Jara, I. Vasilescu. A soft touch: compliant tactile sensors for sensitive manipulation. In *CSAIL Technical Report MIT-CSAIL-TR-2006-014*, 2006.
- R.A. Russell G. Hellard. A robust, sensitive and economical tactile sensor for a robotic manipulator. In *Proc. of Australasian Conference on Robotics and Automation*, pages 100–104, 2002.
- J. Heo, J. Chung, and J. Lee. Tactile sensor arrays using fiber bragg grating sensors. *Sensors and Actuators A: Physical*, 126(2):312–327, 2006.
- S. Hirose and K. Yoneda. Development of optical 6-axial force sensor and its signal calibration considering non linear calibration. In *Proc. IEEE Int. Conf. on Robotics and Automation*, Tsukuba, Japan, 1990.
- K. Kamiyama, K. Vlack, T. Mizota, H. Kajimoto, N. Kawakami, and S. Tachi. Vision-based sensor for real-time measuring of surface traction fields. *Computer Graphics and Applications, IEEE*, 25(1):68–75, 2005.
- S.O. Kasap. *Optoelectronics and Photonics: Principles and Practices*. Prentice Hall, Englewood Cliffs, NJ, 2001.
- C. Melchiorri. Tactile sensing for robotic manipulation. In *Articulated and Mobile Robotics for Services and Technologies (RAMSETE)*, pages 75–102. Springer, 2001.
- G. Palli and C. Melchiorri. Velocity and disturbance observer for non-model based load and friction compensation. In *Proc. Int. Workshop on Advanced Motion Control*, pages 194–199, Trento, Italy, 2008.
- J.K. Salisbury. Interpretation of contact geometries from force measurements. In *Robotics and Automation. Proceedings. 1984 IEEE International Conference on*, pages 240–247, 1984.
- A. Tar and G. Cserey. Development of a low cost 3d optical compliant tactile force sensor. In *Advanced Intelligent Mechatronics (AIM), 2011 IEEE/ASME International Conference on*, pages 236–240, 2011.